Ab initio studies on interactions in K_3C_{60} under high pressure

Jianyu Li,[1] Zhangkai Cao,[1] Jiahao Su,[1] Ruipeng Wang,[2] Haipeng Li,[2] Yusuke Nomura,[3] Xiaosen Yang,[4,*] and Ho-Kin Tang[1,†]

[1]*School of Science, Harbin Institute of Technology, Shenzhen 518055, China*
[2]*School of Materials Science and Physics, China University of Mining and Technology, Xuzhou 221116, China*
[3]*Department of Applied Physics and Physico-Informatics, Keio University, Yokohama 223-8522, Japan*
[4]*Department of Physics, Jiangsu University, Zhenjiang 212013, China*

(Received 20 October 2023; revised 1 February 2024; accepted 10 April 2024; published 23 April 2024)

Fullerene solids doped with alkali metals (A_3C_{60}, A = K, Rb, Cs) exhibit a superconducting transition temperature T_c as high as 40 K, and their unconventional superconducting properties have been a subject of debate. With the application of high pressure on K_3C_{60} and Rb_3C_{60}, experiments demonstrate the decrease of T_c. In this paper, we focus on K_3C_{60} and derive the structure of K_3C_{60} under different pressures based on first-principles calculations, exploring the trends of Coulomb interactions at various pressures. By utilizing the maximally localized Wannier function approach, constrained density functional perturbation theory, and constrained random phase approximation, we construct a microscopic low-energy model near the Fermi level. Our results strongly indicate that, in the K_3C_{60} system, as pressure increases, the effect of phonons is the key to intraorbital electron pairing. The phonon-driven superconducting mechanism is dominant at high pressure.

DOI: 10.1103/PhysRevB.109.134513

I. INTRODUCTION

Since their discovery three decades ago, fullerenes have commanded substantial scientific attention [1–4]. Notably, the intriguing hallmark of these molecules resides in their distinctive geometric structure: C_{60} molecules exhibit the symmetry of an icosahedral group, a symmetry class of paramount significance within the realm of symmetric operations. The recent realization of monolayer fullerene materials [5–12] further underscores the importance of investigating fullerene materials' physical properties, as these insights are pivotal in unlocking their full technological potential.

After solid C_{60} (fullerene crystals) was successfully synthesized, a series of extensive solid-state experiments was conducted, revealing numerous significant physical properties [13–16]. For instance, fcc K_3C_{60} demonstrates metallic behavior, with the resistivity increasing as the temperature rises [13]. A distinct Drude peak is observed in the optical conductivity, and photoemission studies identified a finite density of states near the Fermi level [17–20]. Pressure tuning of light-induced superconductivity in K_3C_{60} has also led to significant progress [21,22]. Measurements of electron spin resonance [23,24] and nuclear magnetic resonance [25–27] indicate a Pauli-like susceptibility behavior in the normal state, which is nearly temperature independent.

A groundbreaking achievement was made by Hebard *et al.* as they successfully identified superconductivity in potassium-doped C_{60}, notably characterizing a superconducting transition at a critical temperature of $T_c = 18$ K [28]. Subsequent investigations into the underlying superconducting mechanisms revealed resemblances to the BCS theory, supported by consistent experiments. These include the confirmation of a full-gap *s*-wave pairing [25,29–31], a reduction in spin susceptibility within the superconducting phase [26], the observation of the Hebel-Slichter peak [32] with nuclear magnetic resonance (NMR) [26,33], and the correlation between the lattice constant and T_c [34].

Moreover, there have been thorough examinations of pressure-induced alterations in T_c [35–37] and the lattice parameter [37,38] within the K_3C_{60} system. In non-Cs-doped C_{60} superconductors, the observation of T_c monotonically decreasing under lattice compression was attributed to the band widening caused by lattice contraction, resulting in a reduction of the density of states at the Fermi level [34,35,38–41]. In the context of the general reduction in T_c under pressure, these experimental findings provide the conditions for further exploration of the superconducting mechanism in K_3C_{60}.

Given the intricate interplay between electronic correlations and complex electron-phonon coupling (EPC), the mechanisms underpinning superconductivity in fullerenes remain contentious. While initial perceptions categorized fullerene superconductors as conventional BCS systems, the discourse has expanded to encompass an array of unconventional theories. These include propositions of polaron-driven superconductivity [42,43], local pairing facilitated by Jahn-Teller phonons and Coulomb repulsion [44,45], the intriguing concept of negative Hund's coupling stabilized by EPC [46,47], and even scenarios of pure electronic pairing [48], among other possibilities.

In this context, our present study initiates an *ab initio* exploration of interactions within the K_3C_{60} system under the influence of elevated pressures. Utilizing experimentally

*yangxs@ujs.edu.cn
†denghaojian@hit.edu.cn

acquired data on lattice constants under various pressures [37], we aim to employ a combination of density functional theory (DFT) and the model-calculation approach [49–51] to compute essential interaction parameters. We will determine the effective Coulomb interaction within the low-energy subspace using the constrained random phase approximation (cRPA) [52]. Additionally, we will calculate partially renormalized phonon frequencies and electron-phonon couplings through the constrained density functional perturbation theory (cDFPT) [53,54]. Our primary objective is to unveil the alterations in physical properties, ranging from electronic characteristics to phonon behavior, caused by pressure fluctuations. By closely examining the pressure-induced modifications in various interaction parameters, we strive to discern the most plausible superconducting mechanism amid the changing pressure conditions.

The rest of this paper is outlined as follows. In Sec. II, we choose the target band and show the low-energy models from *ab initio* calculations. In Sec. III, we calculate the global band structure using DFT and construct maximally localized Wannier orbitals within the low-energy band subspace. Detailed computations are presented in this section. We obtain parameter results for the Coulomb interaction and electron-phonon interaction and analyze their trends with varying pressure. In Sec. IV, we discuss changes in electronic and phononic properties resulting from pressure fluctuations and compare various explanations for the unconventional superconducting mechanism in K_3C_{60}. Finally, we present the conclusion in Sec. V.

II. METHOD AND MODEL

Close to the Fermi energy, the t_{1u} band, which we call the target band, is the focus of our investigation. We use a lattice Hamiltonian encompassing the electron and phonon degrees of freedom specifically associated with the t_{1u} orbitals that was formulated in Refs. [47,55]. Nearly all the excitation processes occur in the t subspace, the subspace which the target bands span (for later use, we define the r subspace as the rest of the Hilbert space). The Hamiltonian assumes the following general form:

$$\begin{aligned}\mathcal{H} = &\sum_{ij\mathbf{k}\sigma} \mathcal{H}^{(0)}_{ij}(\mathbf{k}) c^{\sigma\dagger}_{i\mathbf{k}} c^{\sigma}_{j\mathbf{k}} \\ &+ \sum_{\mathbf{q}\mathbf{k}\mathbf{k}' ij i' j'} \sum_{\sigma\sigma'} U_{ij,i'j'}(\mathbf{q}) c^{\sigma\dagger}_{i\mathbf{k}+\mathbf{q}} c^{\sigma'\dagger}_{j'\mathbf{k}'} c^{\sigma'}_{i'\mathbf{k}'+\mathbf{q}} c^{\sigma}_{j\mathbf{k}} \\ &+ \sum_{ij\mathbf{k}\sigma\mathbf{q}\nu} \sum_{ij} g^{\nu}_{ij}(\mathbf{k},\mathbf{q}) c^{\sigma\dagger}_{i\mathbf{k}+\mathbf{q}} c^{\sigma}_{j\mathbf{k}} (b_{\mathbf{q}\nu} + b^{\dagger}_{-\mathbf{q}\nu}) \\ &+ \sum_{\mathbf{q}\nu} \omega_{\mathbf{q}\nu} b^{\dagger}_{\mathbf{q}\nu} b_{\mathbf{q}\nu}. \end{aligned} \tag{1}$$

This Hamiltonian operates on the fcc lattice, where each lattice site corresponds to a C_{60} molecule. The terms $\mathcal{H}^{(0)}$, U, g, and ω respectively denote the one-body electron Hamiltonian, Coulomb interaction, electron-phonon coupling, and phonon frequency. All these quantities are indexed by Wannier orbitals i, j, i', and j'; spins σ and σ'; momentum $\mathbf{k}$; and $\mathbf{q}$, and the phonons are further distinguished by the branch index ν. To ensure the short-range nature of hopping, we

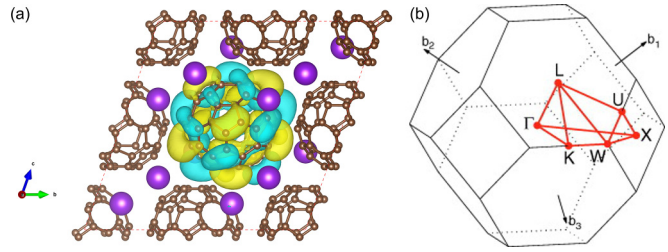

FIG. 1. (a) The atomic structure of K_3C_{60}, which is set at a size of $2 \times 2 \times 2$, and the real-space Wannier function displayed using VESTA software [57]. K atoms are depicted as purple spheres, while C atoms are represented by brown spheres. Positive isosurfaces are highlighted in yellow, while negative isosurfaces are shown in blue. (b) Brillouin zone of the fcc lattice; the path is Γ-*X*-*U*-*K*-Γ-*L*-*K*-*W*-*X*, as described in Ref. [58].

constructed maximally localized Wannier orbitals [56] as the basis [Fig. 1(a)]. Reflecting the molecular nature of solids, the maximally localized Wannier orbitals constructed from the t_{1u} bands are well localized on one molecule and cannot be assigned to specific atoms in the crystal [Fig. 1(a)]. These parameters are determined using state-of-the-art *ab initio* techniques, with a particular emphasis on the utilization of cRPA [52] for the calculation of electron-related terms $U_{ij,i'j'}$ and the cDFPT [53] for the calculation of the phonon-related terms g^{ν}_{ij} and $\omega_{\mathbf{q}\nu}$, where the influence of the high-energy bands is incorporated into the parameter values. Here, we consider only the local part (U_{ph}, U'_{ph}, and J_{ph}) of phonon-mediated electron-electron interactions. This is because the intramolecular electron-phonon coupling plays a dominant role. If nonlocal electron-phonon coupling were strong, the current modeling of electron-phonon coupling would not be valid.

The parameters $\mathcal{H}^{(0)}_{ij}(\mathbf{k})$ represent an on-site energy ($\mathbf{k} = \mathbf{0}$) and hopping integrals ($\mathbf{k} \neq \mathbf{0}$), which are described with translational symmetry as

$$\mathcal{H}^{(0)}_{ij}(\mathbf{k}) = \langle \phi_{i\mathbf{k}} | \mathcal{H}_{\mathrm{KS}} | \phi_{j\mathbf{0}} \rangle, \tag{2}$$

where $|\phi_{i\mathbf{k}}\rangle = c^{\dagger}_{i\mathbf{k}}|0\rangle$ and $\mathcal{H}_{\mathrm{KS}}$ is the Kohn-Sham Hamilton.

To evaluate effective interaction parameters $U_{ij,i'j'}(\mathbf{q})$, we convert $U_{ij,i'j'}(\mathbf{q})$ into the on-site Coulomb repulsion U_{ij} and the exchange interaction J_{ij} and calculate the screened Coulomb interaction W at the low-frequency limit. We first calculate the noninteracting-polarization function χ, excluding polarization processes within the target bands. Note that screening by the target electrons is considered when we solve the effective models, so we have to avoid double counting it when we derive the effective models. With the resulting χ, the W interaction is calculated as $W = (1 - v\chi)^{-1} v$, where v is the bare Coulomb interaction potential $v(\mathbf{r}, \mathbf{r}') = \frac{1}{|\mathbf{r}-\mathbf{r}'|}$. We consider a decomposition of the total irreducible polarization χ^0 into the one involving only the t-subspace electrons χ^0_t and one involving the rest χ^0_r [52]:

$$\chi^0 = \chi^0_t + \chi^0_r.$$

Note that χ^0_r contains not only the processes involving only the r-subspace degrees of freedom but also the ones involving both the t-subspace electrons and the r-subspace electrons.

We define the partially screened Coulomb interaction $W^{(p)}$ as

$$W^{(p)} = \left(1 - v\chi_r^0\right)^{-1} v = \epsilon_r^{-1} v. \tag{3}$$

The on-site Coulomb repulsion U_{ij} and the exchange interaction J_{ij} are evaluated as

$$\begin{aligned} U_{ij} &= \iint d\mathbf{r} d\mathbf{r}' |\phi_{i\mathbf{0}}(\mathbf{r})|^2 W^{(p)}(\mathbf{r}, \mathbf{r}') \left|\phi_{j\mathbf{0}}(\mathbf{r}')\right|^2 \\ &= \frac{4\pi e^2}{N\Omega} \sum_{\mathbf{q}} \sum_{\mathbf{G}\mathbf{G}'} \rho_{ii}(\mathbf{q}+\mathbf{G}) W^{(p)}_{\mathbf{G},\mathbf{G}'}(\mathbf{q}) \rho^*_{jj}(\mathbf{q}+\mathbf{G}') \end{aligned} \tag{4}$$

and

$$\begin{aligned} J_{ij} &= \iint d\mathbf{r} d\mathbf{r}' \phi^*_{i\mathbf{0}}(\mathbf{r}) \phi_{j\mathbf{0}}(\mathbf{r}) W^{(p)}(\mathbf{r}, \mathbf{r}') \phi^*_{j\mathbf{0}}(\mathbf{r}') \phi_{i\mathbf{0}}(\mathbf{r}') \\ &= \frac{4\pi e^2}{N\Omega} \sum_{\mathbf{q}} \sum_{\mathbf{G}\mathbf{G}'} \rho_{ij}(\mathbf{q}+\mathbf{G}) W^{(p)}_{\mathbf{G},\mathbf{G}'}(\mathbf{q}) \rho^*_{ij}(\mathbf{q}+\mathbf{G}'), \end{aligned} \tag{5}$$

respectively, where Ω is the volume of the unit cell and $\rho_{ij}(\mathbf{q}+\mathbf{G})$ is given, with the Wannier-gauge Bloch functions $\psi^{(w)}_{i\mathbf{k}}$, by

$$\rho_{ij}(\mathbf{q}+\mathbf{G}) = \frac{1}{N} \sum_{\mathbf{k}} \left\langle \psi^{(w)}_{i\mathbf{k}+\mathbf{q}} \left| e^{i(\mathbf{q}+\mathbf{G})\cdot\mathbf{r}} \right| \psi^{(w)}_{j\mathbf{k}} \right\rangle. \tag{6}$$

To facilitate a comparative analysis with the cRPA results, we compute interaction parameters using the unscreened case, representing the bare Coulomb interaction. In order to differentiate it from the cRPA results, we refer to this as the "bare" interaction.

In solids, the individual ion can be identified as the κth ion in the pth unit cell, and the direction of the displacement $\alpha = x, y, z$. To evaluate effective electron-phonon-coupling interaction parameters, we use

$$g^{\nu}_{ij}(\mathbf{k}, \mathbf{q}) = \sum_{\kappa\alpha} \sqrt{\frac{\hbar}{2M_\kappa \omega_{\mathbf{q}\nu}}} e^{(p)\alpha}_{\kappa}(\mathbf{q}\nu) \left\langle \phi_{i\mathbf{k}+\mathbf{q}} \left| \frac{\partial V^{(p)}(\mathbf{r})}{\partial u^{\alpha}_{\kappa}(\mathbf{q})} \right| \phi_{j\mathbf{k}} \right\rangle, \tag{7}$$

where we employ the Wannier-gauge for the electrons and the superscript (p) indicates the partially renormalized quantities.

Here, we consider the real-phonon contributions, the intraorbital density-density-type interaction U_{ph}, interorbital density-density-type interaction U'_{ph}, and exchange-type interaction J_{ph}:

$$U_{\mathrm{ph}} = -\frac{1}{N_{\mathbf{q}}} \sum_{\mathbf{q}\nu} \frac{2\left|\tilde{g}^{(p)}_{ii}(\mathbf{q}, \nu)\right|^2}{\omega^{(p)}_{\mathbf{q}\nu}}, \tag{8}$$

$$U'_{\mathrm{ph}} = -\frac{1}{N_{\mathbf{q}}} \sum_{\mathbf{q}\nu} \frac{2\tilde{g}^{(p)}_{ii}(\mathbf{q}, \nu)\tilde{g}^{(p)*}_{jj}(\mathbf{q}, \nu)}{\omega^{(p)}_{\mathbf{q}\nu}}, \tag{9}$$

$$\begin{aligned} J_{\mathrm{ph}} &= -\frac{1}{N_{\mathbf{q}}} \sum_{\mathbf{q}\nu} \frac{2\tilde{g}^{(p)}_{ij}(\mathbf{q}, \nu)\tilde{g}^{(p)*}_{ij}(\mathbf{q}, \nu)}{\omega^{(p)}_{\mathbf{q}\nu}} \\ &= -\frac{1}{N_{\mathbf{q}}} \sum_{\mathbf{q}\nu} \frac{2\tilde{g}^{(p)}_{ij}(\mathbf{q}, \nu)\tilde{g}^{(p)*}_{ji}(\mathbf{q}, \nu)}{\omega^{(p)}_{\mathbf{q}\nu}}, \end{aligned} \tag{10}$$

where the orbital dependences of U_{ph}, U'_{ph}, and J_{ph} do not exist by symmetry and $\tilde{g}^{(p)}_{ij}(\mathbf{q}, \nu)$ is calculated as

$$\tilde{g}^{(p)}_{ij}(\mathbf{q}, \nu) = \frac{1}{N_{\mathbf{k}}} \sum_{\mathbf{k}} g^{(p)\nu}_{ij}(\mathbf{k}, \mathbf{q}). \tag{11}$$

III. RESULT

A. Calculation details

We constructed maximally localized Wannier orbitals (MLWOs; Fig. 1) from the DFT t_{1u} band and calculated the model parameters in the lattice Hamiltonian [Eq. (1)] as described in Sec. II. We employed the local density approximation (LDA) exchange-correlation functional with the parametrization by Perdew, Burke, and Ernzerhof and employed the Troullier-Martins conservative pseudopotentials within the Kleinman-Bylander representation. The reference configurations used to generate the pseudopotentials for C and K are $(2s)^2(2p)^2$ and $(3p)^6(4s)^0(3d)^0$, respectively.

A partial core correction was applied to the pseudopotential for the alkali metal K. The unit cell volume data for K_3C_{60} at different pressures were obtained from experimental sources [37]. Calculations were performed using the open-source software QUANTUM ESPRESSO [59–61] and RESPACK [62–67]. We performed the structure optimization by fixing the lattice constants to the values employed [37] and ignoring the orientational disorder of C_{60} molecules.

In DFT calculations, the crystal lattice is defined as a type-2 Bravais lattice, with the lattice parameter a determined from Fig. 2(a). The calculation includes 350 electronic bands. Electron occupation numbers are determined using the "smoothing" method with a Gaussian smoothing of 0.025 Ry. In our Wannier orbital calculations, we specified the following parameters: a crystal cell with a multiplicity of 2, a computation for three Wannier orbitals, and an energy window ranging from $E_{\mathrm{F}} - 0.5$ to $E_{\mathrm{F}} + 0.5$ eV (E_{F} is the Fermi energy). We employed a set of six initial Gaussian functions as a foundational basis. Moreover, we defined Gaussian function coefficient matrices for distinct orbital types, such as p_x, p_y, and p_z. For example, in the case of the p_x orbital, the coefficient matrix comprises four values: 1.0, −0.243, 0.243, and 0.243, which represent the weights assigned to each Gaussian function utilized in constructing the p_x orbital. Similarly, p_y and p_z orbitals possess analogous coefficient matrices for specifying their Gaussian function weights. Additionally, we established a path for symmetric **k**-point interpolation, encompassing specific high-symmetry points: Γ (0, 0, 0), X (0.5, 0, 0.5), U (0.625, 0.25, 0.625), K (0.375, 0.375, 0.75), L (0.5, 0.5, 0.5), and W (0.5, 0.25, 0.75) [Fig. 1(b)]. Then, we calculated the band structure for the optimized structure.

In order to maximize the utilization of computational resources, different cutoff energies for wave functions and charge densities, as well as **k**-point sampling grids, were set because the calculation requirements vary when computing Coulomb interactions using the cRPA method and electron-phonon interactions using the cDFPT method. In the calculation of effective parameters for Coulomb interaction, the wave function and charge density were truncated with kinetic energy cutoffs of 36 and 144 Ry, respectively. A

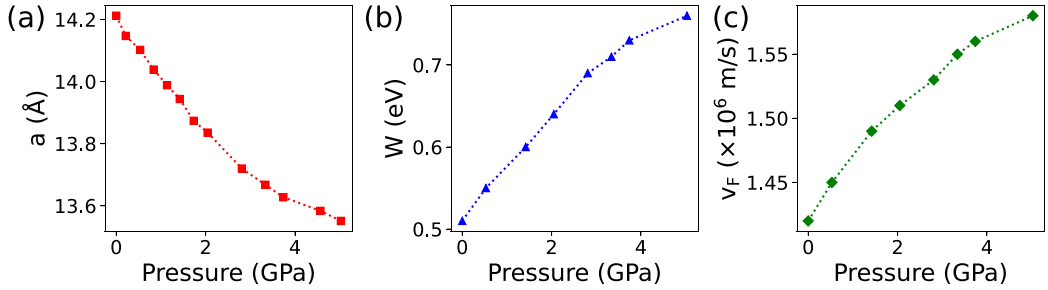

FIG. 2. The pressure dependence of (a) lattice constant a, (b) bandwidth W, and (c) Fermi velocity v_F. We fix the lattice constants to the experimental values [37] and calculate the bandwidth of the t_{1u} band using QUANTUM ESPRESSO [59–61]. We combine Eq. (14) to obtain the Fermi velocity from the energy band results.

k-point sampling grid of $5 \times 5 \times 5$ **k** points was utilized. But in the calculation of effective parameters for electron-phonon interactions, the cutoff energy for the wave functions was set to 50 Ry, and we employed $4 \times 4 \times 4$ **k** points. The cDFPT calculations were performed with a $2 \times 2 \times 2$ **q** mesh.

B. Band structure

The C_{60} solid possesses a three-dimensional crystal structure [68,69] owing to the relatively isotropic shape of the C_{60} molecule. The centers of these molecules form an fcc lattice. Considering that undoped C_{60} constitutes a molecular solid, an insightful initial approach to comprehend its electronic structure is to examine the molecular limit. In this limit, numerous molecular orbitals degenerate due to the high symmetry inherent in the molecule itself: specifically, the C_{60} molecule boasts the fivefold-degenerate highest occupied molecular orbital (HOMO), threefold-degenerate lowest unoccupied molecular orbital (LUMO), and threefold-degenerate LUMO + 1 orbitals, denoted as h_u, t_{1u}, and t_{1g} orbitals, respectively, based on their symmetry properties. In the context of a solid, these orbitals acquire a dispersion as a result of electron transfers taking place between the molecules. However, owing to the relatively small magnitude of the transfer integral, the bandwidth of each orbital remains narrow (typically around ∼0.5 eV). Consequently, there is minimal overlap observed between the bands associated with different molecular orbitals. Meanwhile, the C_{60} solid manifests as a band semiconductor in which the LUMO t_{1u} band remains unoccupied, while the HOMO h_u band is fully populated.

In fcc K_3C_{60}, each alkali atom donates about one electron to the t_{1u} band, so the t_{1u} band becomes half filled. As a result, K_3C_{60} is no longer a semiconductor; instead, it exhibits partially metallic characteristics. Figure 3 illustrates the computed band structures of fcc K_3C_{60} at various pressure levels within the framework of LDA. These compounds exhibit shared characteristics in their band structures; particularly notable is the presence of narrow bands in proximity to the Fermi level which are well isolated from other bands. Within K_3C_{60}, a set of threefold-degenerate states, known as the t_{1u} band, exists which occupies a prominent position in the vicinity of the Fermi level. This distinctive feature renders them particularly suitable for selection as target bands in the construction of an effective model.

We show in Fig. 4 the calculated density of states (DOS) of the t_{1u} band for fcc K_3C_{60}. The DOS configuration profile shows only a relatively small change, in which the profile generally obeys the DOS behavior of the Fermi gas. This suggests we can use the Fermi gas model to quantify Fermi parameters. For the Drude model, we define the density of states $N(E)$, Fermi energy E_F, and Fermi velocity v_F:

$$N(E) = \frac{2V}{(2\pi)^2}\left(\frac{2m^*}{\hbar^2}\right)^{3/2} E^{1/2}, \tag{12}$$

$$E_F = \hbar^2 \frac{k_F^2}{2m^*}, \tag{13}$$

$$v_F = \hbar \frac{k_F}{m^*}. \tag{14}$$

We find that $N(E) \propto v_F$ and $E_F \propto v_F^2$, demonstrating a consistent alignment between theoretical and computational trends. Increasing pressure causes a reduction in the lattice constant of K_3C_{60} [Fig. 2(a)], leading to an upward shift of the Fermi level and an increase in the Fermi velocity. Additionally, alterations in lattice constant impact the electronic band structure, resulting in a wider bandwidth and influencing the density of states. Both bandwidth W and Fermi velocity v_F exhibit a monotonic increase as the lattice constant decreases; W rises from 0.51 to 0.76 eV [Fig. 2(b)], representing an approximately 50% increase, and v_F rises from 1.42×10^6 to 1.58×10^6 m/s [Fig. 2(c)], representing an approximately 11% increase.

C. Coulomb interaction parameters of K_3C_{60}

In this section, we analyze the effective Coulomb interaction parameters for K_3C_{60}. Specifically, we focus on the parameters $U = U_{ii}(\mathbf{0})$, $U' = U_{ij}(\mathbf{0})$, and $J = J_{ij}(\mathbf{0})$, where $i \neq j$, with $U_{ij}(\mathbf{R})$ in Eq. (4) and $J_{ij}(\mathbf{R})$ in Eq. (5). U is the intraorbital Coulomb interaction, U' is the interorbital interaction, and J is the exchange interaction. Figure 5 shows our calculated interaction parameters U, U', and J with two screening levels (bare and cRPA). It can be observed that the values of effective interaction parameters decrease due to the screening process. For instance, at 0 GPa, the bare Coulomb repulsion for K_3C_{60} is approximately 3.32 eV, but if we consider the cRPA screening effects, this value decreases to around 0.83 eV.

Figure 6 shows the inverse dielectric matrix $\{\epsilon^{-1}_{\mathbf{GG}}(\mathbf{q}, \omega)\}$; the macroscopic dielectric constant is defined as

$$\epsilon_M^{\mathrm{cRPA}} = \lim_{\mathbf{Q}\to 0, \omega \to 0} \frac{1}{\epsilon_{\mathbf{GG}}^{\mathrm{cRPA}^{-1}}(\mathbf{q}, \omega)}, \tag{15}$$

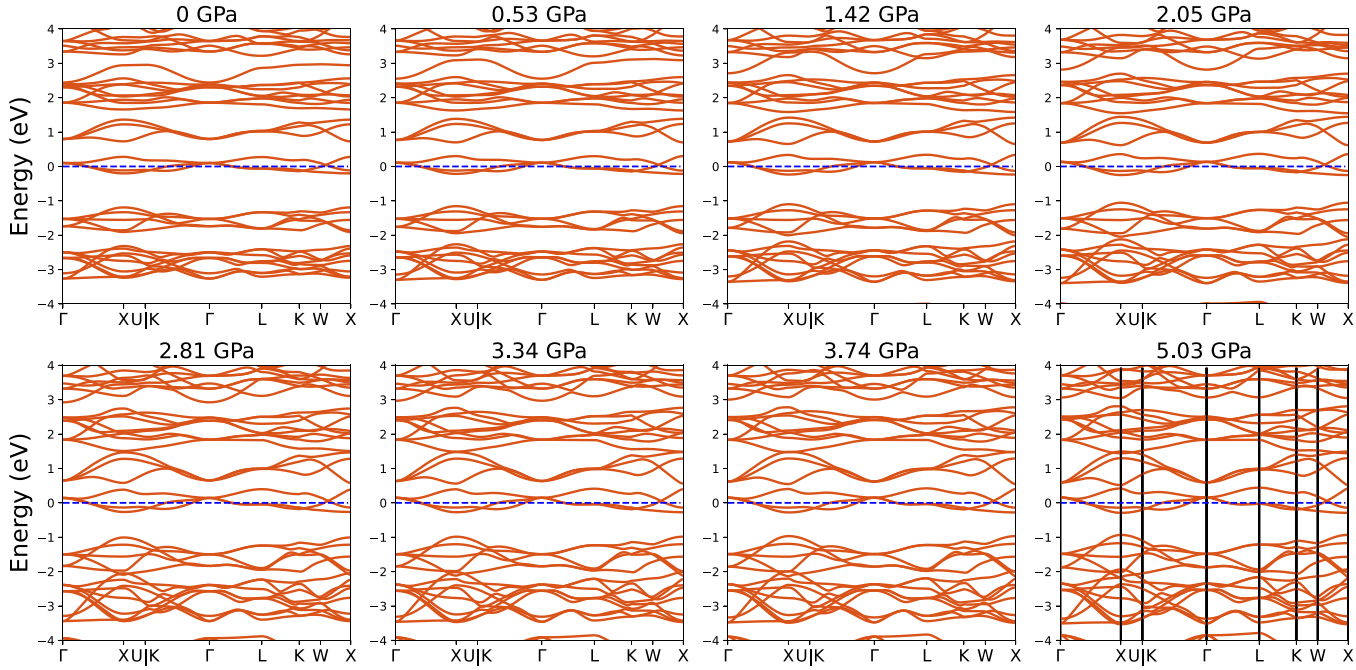

FIG. 3. Calculated *ab initio* electronic band structure of fcc K_3C_{60} at different pressures. The pressure parameters are set as 0, 0.53, 1.42, 2.05, 2.81, 3.34, 3.74, and 5.03 GPa. The horizontal axis is labeled with the special points in the Brillouin zone: Γ (0, 0, 0), *X* (0.5, 0, 0.5), *U* (0.625, 0.25, 0.625), *K* (0.375, 0.375, 0.75), *L* (0.5, 0.5, 0.5), and *W* (0.5, 0.25, 0.75). Fermi energy is depicted as blue dashed lines.

where ω is the frequency and $\mathbf{Q} = \mathbf{q} + \mathbf{G}$, with $\mathbf{q}$ being the wave vector in the first Brillouin zone and $\mathbf{G}$ being the reciprocal lattice vector. Figure 5(d) presents our calculated cRPA-macroscopic-dielectric constant $\epsilon_M^{\mathrm{cRPA}}$ in Eq. (15). The diagonal elements of the inverse dielectric matrix demonstrate lower values with increasing pressure (Fig. 6), eventually converging to 1 with increasing $|\mathbf{q} + \mathbf{G}|$ (Fig. 6, inset).

Figure 7 summarizes the results of the cRPA calculations: the on-site Coulomb repulsion $\bar{U}$ averaged over the ML-WOs derived from the target band, the off-site interaction $\bar{V}$ averaged over the nearest-neighbor sites, the on-site exchange interaction J, the ratio $\bar{U}/W$, and the ratio $(\bar{U} - \bar{V})/W$, which measures the correlation strength in the system.

The metal-insulator transition in a correlated system is commonly analyzed through the U/W ratio [70]. In a solid with approximately one electron per lattice site, the emergence of a Mott-insulating state occurs when the Coulomb

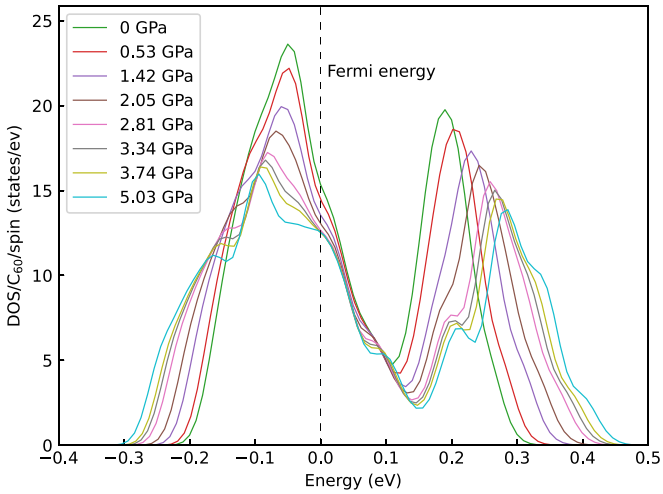

FIG. 4. Our calculated density of states (DOS) for the t_{1u} band of fcc K_3C_{60} at different pressures. The pressure parameters are set as 0, 0.53, 1.42, 2.05, 2.81, 3.34, 3.74, and 5.03 GPa.

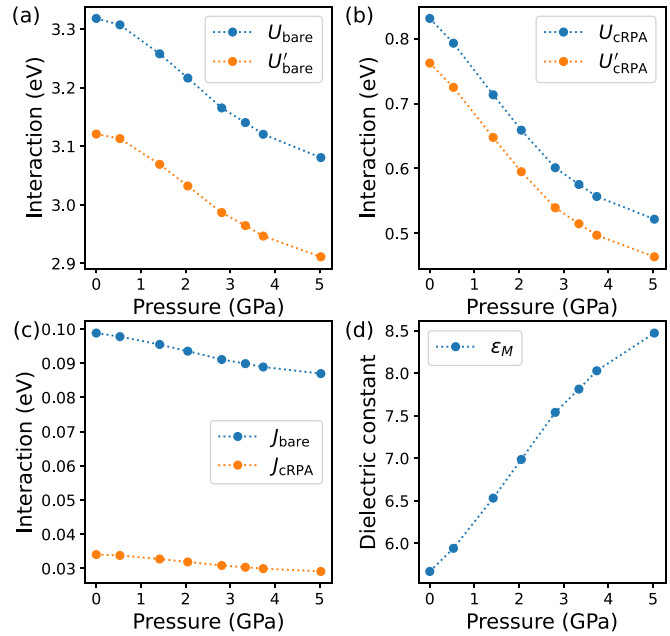

FIG. 5. (a)–(c) U, U', and J with different screening levels [unscreened (bare) and constrained RPA (cRPA)]. For bare and cRPA U, U', and J values, the units are given in eV. (d) ϵ_M, the cRPA-macroscopic-dielectric constant in Eq. (15).

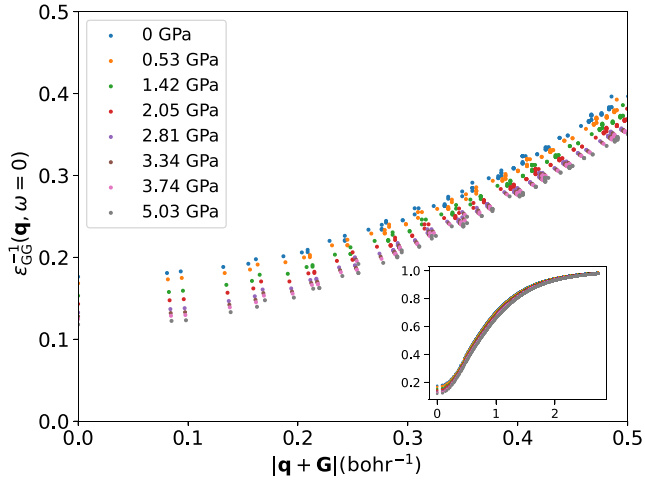

FIG. 6. Diagonal terms of the inverse dielectric matrix for all $\mathbf{q}$ points $\epsilon^{-1}_{\mathbf{GG}}(\mathbf{q}, \omega)$ at the first frequency $\omega = 0$. The horizontal axis is limited within the range of 0 to 0.5 bohr^{-1}, where it represents $|\mathbf{q} + \mathbf{G}|$. Inset: The horizontal axis represents the entire range of $|\mathbf{q} + \mathbf{G}|$.

repulsion U surpasses the one-particle bandwidth W. Conversely, when $U/W \ll 1$, metallic behavior is expected. In situations where $U/W \gg 1$, the substantial energy cost of having one site doubly occupied impedes the free mobility of electrons, resulting in electron localization. Consequently, a first-order metal-insulator transition takes place at a critical U/W ratio close to 1.

Despite K_3C_{60} materials exhibiting relatively high $\bar{U}/W$ values (1.6 without pressure), they manifest metallic behavior rather than the anticipated Mott-insulating behavior [see Fig. 7(d)]. One contributing factor is the inherent frustration in the fcc lattice, which can stabilize the highly correlated metallic state by elevating the critical ratio to even higher values. In contrast, nonfrustrated topologies, such as those based on bcc packing, feature a much smaller critical ratio $(U/W)_c \cong 1.3$ [71] compared to the fcc counterparts.

Note that the net interaction is estimated as $\bar{U} - \bar{V}$ based on the analysis of the extended Hubbard model. Throughout the entire process, the relationship $U' \sim U - 2J$ remains valid. As pressure increases, all parameters exhibit varying degrees of reduction, with the on-site Coulomb repulsion being notably affected by pressure. Specifically, $\bar{U}$ decreases from 0.80 to 0.50 eV, representing a decrease of approximately 40%. The value of J undergoes a relatively minor change, decreasing from 0.034 to 0.029 eV, corresponding to a decrease of approximately 15%. Additionally, $\bar{V}$ decreases from 0.24 to 0.16 eV, approximately declining by 31%. $\bar{U}$ is approximately 3 times $\bar{V}$ and 20 times J. $\bar{U}$ and $\bar{V}$ decrease almost synchronously with increasing pressure, while the rate of decrease in J with pressure is slower than that of $\bar{U}$ and $\bar{V}$. In terms of ratios, $\bar{U}/J$ decreases from 23.4 to 17.0, while $\bar{V}/J$ only decreases from 7.0 to 5.7.

In general, a small value of J tends to favor low-spin states, consistent with experimental observations. It is worth mentioning that there is a proposal suggesting that the Jahn-Teller coupling may exert greater influence than Hund's rule coupling J and, when coupled with a sufficiently large U, may lead to the emergence of superconductivity. We will discuss this pertinent topic in Sec. IV. The ratio $(\bar{U} - \bar{V})/W$, which measures the correlation strength in the system, shows a simple monotonic decrease with the application of pressure. It is noteworthy that at 0 GPa, the value of $(\bar{U} - \bar{V})/W$ is approximately 1, suggesting the potential for C_{60} superconductors to be strongly correlated electronic systems. The results at 0 GPa are consistent with $(\bar{U} - \bar{V})/W \sim 1$ [55] exhibited by other C_{60} superconductors. However, as pressure increases, this value gradually decreases, indicating a departure from a strongly correlated electronic system.

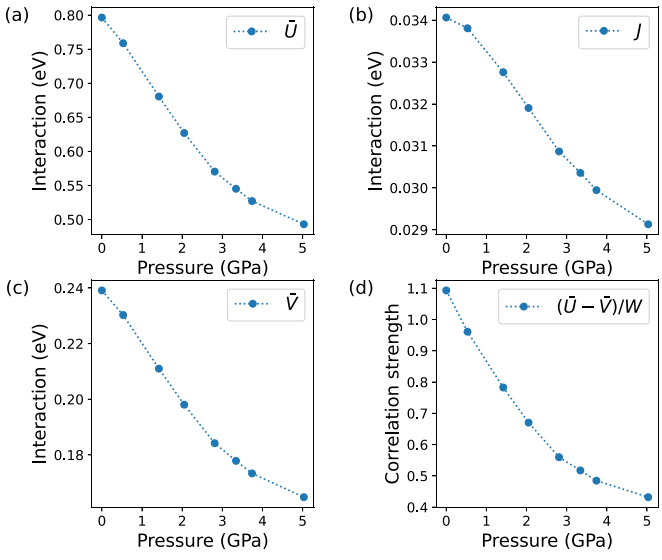

FIG. 7. Pressure dependence of (a) the average of the on-site effective Coulomb repulsion $\bar{U}$, (b) the on-site effective exchange interaction J, (c) the average of the off-site effective Coulomb repulsion between neighboring sites $\bar{V}$, and (d) the correlation strength $(\bar{U} - \bar{V})/W$, which are derived using the cRPA method.

D. Electron-phonon interactions and phonon frequencies

The phonon modes associated with K_3C_{60} that have the potential to interact with the t_{1u} electrons can be categorized into distinct classes, including libration modes, intermolecular modes, optical modes involving alkali cations and C_{60}^{3-} anions, and intramolecular modes [72–76]. For the librations, which involve rigid rotations of the molecules, only the hopping between the molecules is influenced; the coupling observed is only consistent with small values of $\lambda \leqslant 0.08$ [77]. For the intermolecular modes, from the displacement of the band structure energies, $\lambda \sim 0.01$ was estimated for these modes [78]. For alkali-metal phonon modes, the energy is ~0.013, and $\lambda \sim 0.004$ [79]. For intramolecular modes, all λ of the phonon modes exceed 0.01, as shown in Fig. 8. Therefore, our primary focus is on investigating the characteristics of intramolecular phonons.

Given the high symmetry of the C_{60} molecule, only specific types of intramolecular phonon modes can couple with the t_{1u} electrons due to symmetry considerations. If we consider the ideal icosahedral symmetry of the isolated C_{60} molecule, a total of $60 \times 3 - 6 = 174$ intramolecular vibrational modes exist (where the subtraction of six modes pertains to the molecule's translational and rotational degrees of freedom).

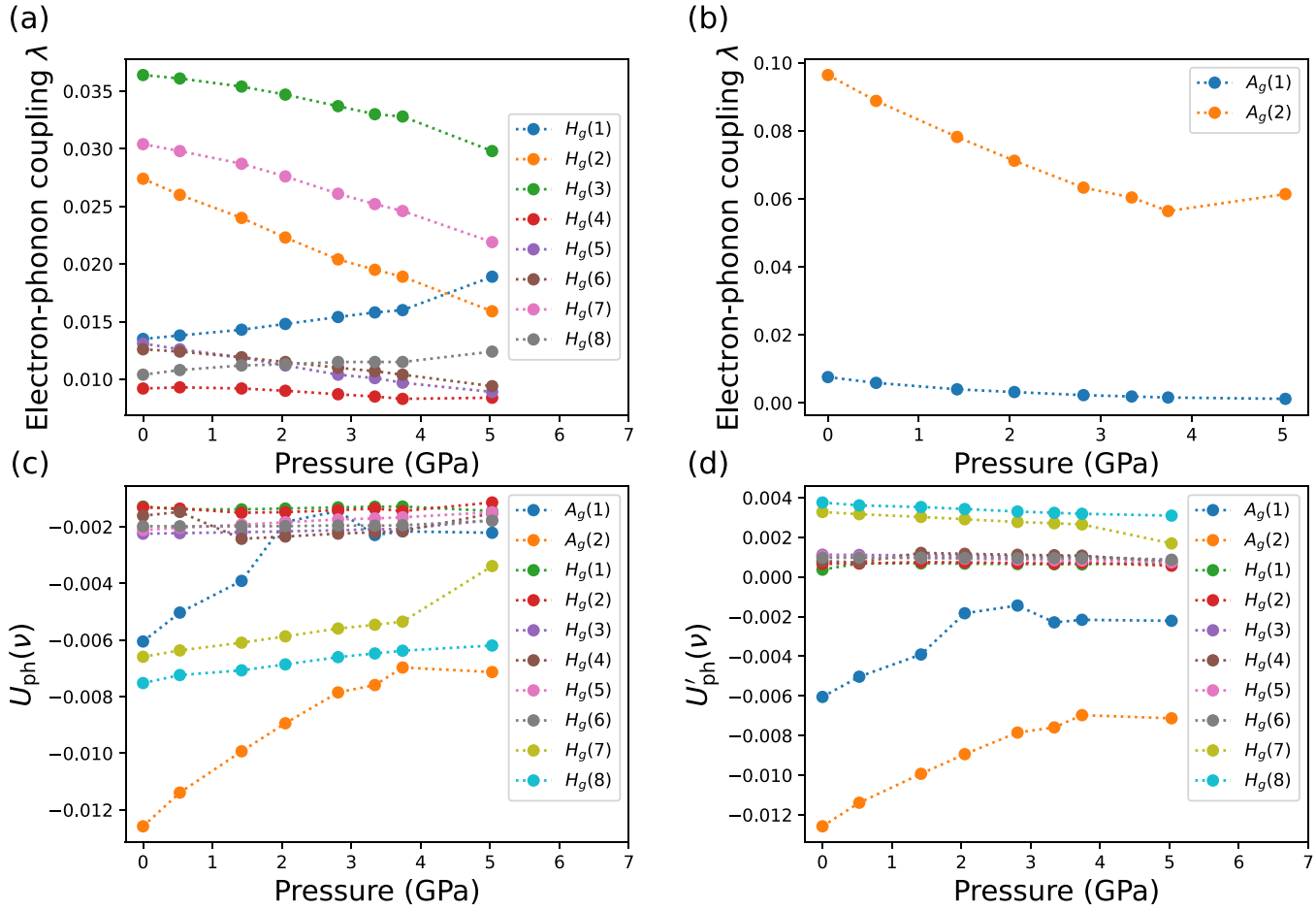

FIG. 8. Partially renormalized electron-phonon coupling parameter for different phonon modes at the Γ point calculated using the cDFPT method. The phonon modes are as follows: (a) $H_g(1)$–$H_g(8)$ and (b) $A_g(1)$ and $A_g(2)$. The mode decomposition of phonon-mediated interactions (c) $U_{ph}(\nu)$ and (d) $U'_{ph}(\nu)$ as a function of pressure.

These modes are further categorized into two A_g modes, one A_u mode, three T_{1g} modes, four T_{1u} modes, four T_{3g} modes, five T_{3u} modes, six G_g modes, six G_u modes, eight H_g modes, and seven H_u modes.

The $A_{g(u)}$ modes exhibit no degeneracy, whereas the $T_{1g(u)}$ and $T_{3g(u)}$ modes, the $G_{g(u)}$ modes, and the $H_{g(u)}$ modes possess threefold, fourfold, and fivefold degeneracies, respectively. Among the intramolecular modes, only the phonon modes with A_g and H_g symmetries exhibit finite electron-phonon couplings to the t_{1u} electrons [80,81].

Table I summarizes our calculated partially renormalized phonon frequencies of all modes at the Γ point under different pressures. High phonon frequencies up to ∼1500 cm^{-1} (∼0.2 eV) can be ascribed to the stiff C–C bonds and the lightness of the carbon atoms. Note that these frequencies are inputs for the low-energy solvers and thus cannot be directly compared with the experimentally observed frequencies. In general, the electron-phonon coupling of the individual mode is not large (see Fig. 8), while the accumulation of the con-

TABLE I. Partially renormalized phonon frequencies of different modes at the Γ point calculated using the cDFPT method. The units are cm^{-1}(1 eV = 8065.54 cm^{-1}).

Pressure (GPa)	$H_g(1)$	$H_g(2)$	$H_g(3)$	$H_g(4)$	$H_g(5)$	$H_g(6)$	$H_g(7)$	$H_g(8)$	$A_g(1)$	$A_g(2)$
0	259.41	427.28	685.73	779.26	1114.59	1273.56	1402.96	1531.60	504.82	1503.33
0.53	260.77	429.27	685.52	781.82	1117.53	1277.27	1407.12	1534.45	509.91	1504.94
1.42	262.92	432.06	685.25	785.49	1121.59	1282.41	1413.03	1538.64	514.54	1507.33
2.05	264.71	434.33	684.98	788.66	1124.99	1287.02	1418.17	1542.50	518.17	1509.58
2.81	266.85	437.14	684.52	792.61	1129.16	1292.71	1424.41	1547.37	522.46	1512.30
3.34	267.89	438.62	684.22	794.29	1130.64	1294.10	1427.68	1549.32	525.02	1514.18
3.74	268.91	439.71	684.05	796.28	1132.94	1297.92	1430.22	1552.10	527.33	1515.02
5.03	271.29	450.40	686.52	777.20	1104.26	1256.63	1374.34	1506.26	520.53	1453.92

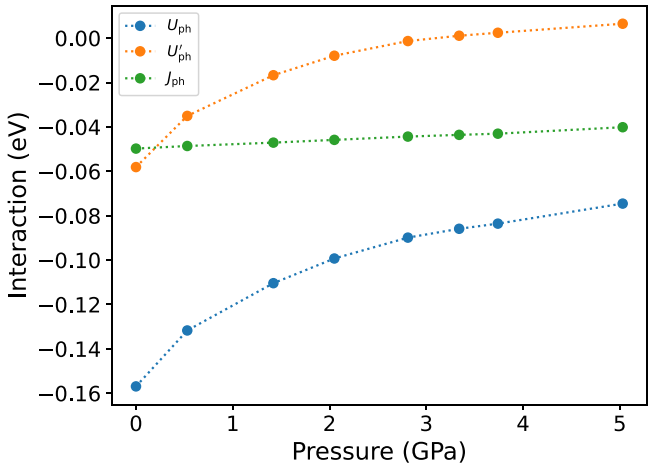

FIG. 9. Pressure dependence of the effective phonon-mediated interaction. U_{ph} is the intraorbital density-density-type interaction, U'_{ph} is the interorbital density-density-type interaction, and J_{ph} is the exchange-type interaction.

tributions leads to a total electron-phonon coupling of $\lambda \sim 0.5$–1.0 [82].

The values of U_{ph} and U'_{ph} are given by the sum of contributions from phonon modes:

$$U'_{ph} = \sum_{\nu} U'_{ph}(\nu), \tag{16}$$

$$U'_{ph}(\nu) = -\frac{1}{N_{\mathbf{q}}} \sum_{\mathbf{q}} \frac{2\tilde{g}^{(p)}_{ii}(\mathbf{q},\nu)\tilde{g}^{(p)*}_{jj}(\mathbf{q}\nu)}{\omega^{(p)}_{\mathbf{q},\nu}}. \tag{17}$$

In Figs. 8(a) and 8(b), we can visually observe the trends of various phonon modes as they change with pressure. With increasing pressure, the majority of phonon modes exhibit a decreasing trend in their intensities, with the exception of the $H_g(1)$ and $H_g(8)$ modes. This observed trend aligns with the overall decrease in phonon coupling strengths as the pressure increases. In Figs. 8(c) and 8(d), we plot $U_{ph}(\nu)$ and $U'_{ph}(\nu)$, respectively, for the A_g and H_g modes as a function of pressure. $U'_{ph}(\nu)$ for A_g modes decreases with pressure, while $U'_{ph}(\nu)$ for H_g modes undergoes relatively small changes.

Figure 9 summarizes the values of the static parts. We also find that the relation $U'_{ph} \sim U_{ph} - 2J_{ph}$ holds well. The negative values of U_{ph}, U'_{ph}, and J_{ph} indicate that the interactions are attractive. Therefore, they will compete with the repulsive on-site Coulomb interactions. It is evident that an increase in pressure leads to a reduction in the absolute magnitudes of U_{ph} and J_{ph}. The weakening trend is consistent for intraorbital density-density-type interactions and exchange-type interactions. Additionally, the magnitude of U'_{ph} decreases to approximately 3 GPa before undergoing a sign reversal, transitioning from negative to positive. This sign change indicates a gradual transition from attraction to repulsion in the interorbital density-density-type interactions. As for the density-density channel, since the Coulomb interaction U for the t_{1u} electrons [see Fig. 7(a)] is approximately 5 times larger in magnitude than electron-phonon coupling U_{ph}, the repulsive Coulomb interaction dominates over the phonon-mediated attraction. However, remarkably, the situation changes for the exchange-type interaction: at 0 GPa the absolute values of $|J_{ph}| \sim 0.05$ eV are larger than those of Hund's coupling $J \sim 0.034$ eV [see Fig. 7(b)]. This indicates that, effectively, negative exchange interactions are realized. Thus, the systems will obey the inverted Hund's rule, which favors the low-spin state rather than the high-spin state. This fact naturally explains the origin of the low-spin state observed in the Mott-insulating phase [83].

On the other hand, the enhancement of the negative J_{ph} is due to the strong coupling between the Jahn-Teller modes and the t_{1u} electrons. As already mentioned in the discussion above, the Jahn-Teller H_g modes are the non-density-type electron-phonon coupling, and A_g modes are density-type electron-phonon coupling. This shows the H_g modes contribute to J_{ph}, and the A_g modes do not contribute. We focus our attention on the behavior of the H_g and A_g modes, as they play key roles in these interactions. Notably, A_g modes predominantly contribute to $|U_{ph}|$, and their trends exhibit substantial similarity. Conversely, H_g modes contribute primarily to $|J_{ph}|$, and it is evident that the trends of the $H_g(2)$–$H_g(7)$ modes are largely consistent with $|J_{ph}|$, although the intensities of the $H_g(1)$ and $H_g(8)$ modes increase as pressure decreases.

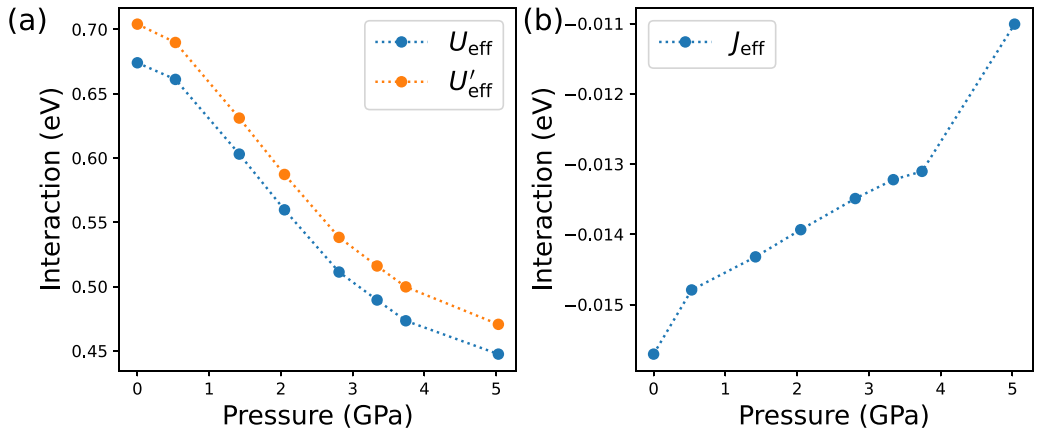

FIG. 10. Pressure dependence of effective interactions $U_{eff}(U + U_{ph})$, $U'_{eff}(U' + U'_{ph})$, and $J_{eff}(J + J_{ph})$. $U[U_{ph}]$, $U'[U'_{ph}]$, and $J[J_{ph}]$ are the intraorbital, interorbital, and exchange components of the cRPA Coulomb (cDFPT phonon-mediated) interactions, respectively.

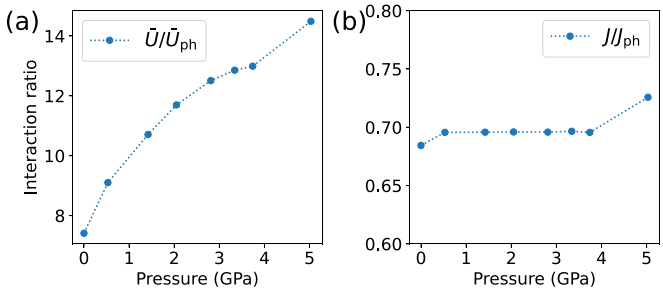

FIG. 11. Pressure dependence of the comparison of effective interactions. $\bar{U}[\bar{U}_{\rm ph}]$ and $J[J_{\rm ph}]$ are the on-site effective Coulomb repulsion and exchange components of the cRPA Coulomb (DFPT phonon-mediated) interactions, respectively.

In Figs. 8(c) and 8(d), the contributions of the A_g modes become more prominent as pressure increases compared to other modes. The decrease in $U'_{\rm ph}(\nu)$ for A_g modes will eventually result in the reversal of the interorbital density-density-type interaction $U'_{\rm ph}(\nu)$ from attraction to repulsion.

E. Effective interactions

Figure 10 shows the pressure dependence of the effective interactions between the t_{1u} electrons ($U_{\rm eff} = U + U_{\rm ph}$, $U'_{\rm eff} = U' + U'_{\rm ph}$, $J_{\rm eff} = J + J_{\rm ph}$), which are given by the sum of the Coulomb U, U', and J and the retarded phonon-mediated interactions $U_{\rm ph}$, $U'_{\rm ph}$, and $J_{\rm ph}$. In the context of K_3C_{60} subjected to variable external pressure conditions, several notable observations have emerged. First, it has been observed that both $U_{\rm eff}$ and $U'_{\rm eff}$ remain positive across the entire range of pressures studied, exhibiting substantial variations as their values decrease from 0.7 to 0.45 eV. Notably, these two parameters exhibit a highly synchronized trend, demonstrating a strong degree of synchronicity. Second, the effective exchange interaction parameter $J_{\rm eff}$ consistently takes negative values under all pressure conditions, with its variation confined to a narrow range, specifically within the limits of -0.016 to -0.011 eV. It is pertinent to note that $U_{\rm eff}$ and $U'_{\rm eff}$ exhibit pronounced repulsive tendencies throughout the studied pressure range which are greater than the attractive tendencies exhibited by $J_{\rm eff}$.

Furthermore, the transition of $J_{\rm eff}$ to negative values is attributed to the contributions from phonons. Within the parameter regime where $J_{\rm eff}$ becomes negative, $U'_{\rm eff}$ is observed to marginally surpass $U_{\rm eff}$, indicating that the interorbital repulsion is slightly greater than the intraorbital repulsion across all pressure conditions. This scenario favors electron pairing within the orbitals, consistent with the conclusions drawn regarding intraorbital pairs [47,84–87].

Figure 11 illustrates the pressure-induced variations in the strengths of the Coulomb interaction and the electron-phonon interaction parameters. In particular, it compares the behavior of on-site effective interaction $\bar{U}$ with that of the phonon-mediated interaction $U_{\rm ph}$. Notably, $\bar{U}$ exhibits a slower rate of reduction compared to $U_{\rm ph}$. This implies that as pressure increases, the intraorbital electron repulsion decreases at a slower rate than the intraorbital electron-phonon attraction. On the other hand, the exchange interaction parameter J exhibits a lower sensitivity to pressure variations. Unlike $\bar{U}$, it does not display pronounced changes with increasing pressure.

IV. DISCUSSION

We carried out a fully *ab initio* study of all the interactions of a multiorbital Hubbard model coupled with phonons computed from first principles with only the information on the atomic positions. In our study, we unveiled changes in electronic and phononic properties induced by pressure fluctuations and compared several explanations for the unconventional superconducting mechanism in K_3C_{60}. Referring to the experimental trend of decreasing T_c in K_3C_{60} as pressure increases [3,35], we make the following observations:

(1) As pressure increases, the strength of the Coulomb interaction consistently surpasses that of the electron-phonon interaction, although both exhibit decreasing trends. Furthermore, phonon-mediated interaction decreases in strength more rapidly than Coulomb interaction. The concurrent weakening of the superconducting phase and phonon interactions aligns well with the proposition that local pairing with Jahn-Teller phonons assisted by Coulomb repulsion predominates as the superconducting mechanism [44,45,88] in K_3C_{60}. This highlights the impact of phonon interactions on the superconducting mechanism, even though the phonon interaction strength in K_3C_{60} is relatively modest due to the dominant role of strong Coulomb interactions in suppressing kinetic energy.

(2) Through band structure calculations, we assert that the primary source of electrons within K_3C_{60} relies on the t_{1u} band. The density of states plot in Fig. 4 reveals that the t_{1u} band is entirely contributed by electrons from the carbon atoms, independent of potassium atoms. This observation indicates that the hypothesis suggesting that potassium ion phonon modes exert a strong attractive force on electrons on C_{60} sufficient to overcome Coulomb repulsion and induce superconductivity [89] is incorrect. Instead, the role of potassium atoms is to donate electrons to the C_{60} HOMO orbitals. C_{60} solids are semiconducting, with a finite gap between HOMO and LUMO orbitals. Doping is required to realize a metallic state. Each potassium atom donates one electron to the C_{60} molecules; then C_{60} becomes a $3-$ anion, and the LUMO orbital becomes half filled. Also, the potassium atom acts as a chemical pressure, so by changing the alkali species, the lattice constant can be changed.

(3) In K_3C_{60}, when considering only the Coulomb interaction in isolation, we observe that U is greater than U'. However, upon incorporating electron-phonon interactions, denoted as $U_{\rm ph}$ and $U'_{\rm ph}$, we discern that $U_{\rm eff}$ becomes smaller than $U'_{\rm eff}$. This observation forms the foundational explanation for electron pairing. Despite the relatively modest strength of phonon interactions within K_3C_{60}, the robust Coulomb interactions effectively curtail the kinetic energy of electrons. This, in turn, facilitates the interorbital tunneling of electron pairs through pair-hopping interactions, which is an indispensable mechanism for the emergence of superconductivity. Throughout the entire process, both $U_{\rm eff}$ and $U'_{\rm eff}$ decrease with increasing pressure, with $U_{\rm eff}$ consistently being less than $U'_{\rm eff}$. This indicates that interorbital Coulomb interactions are

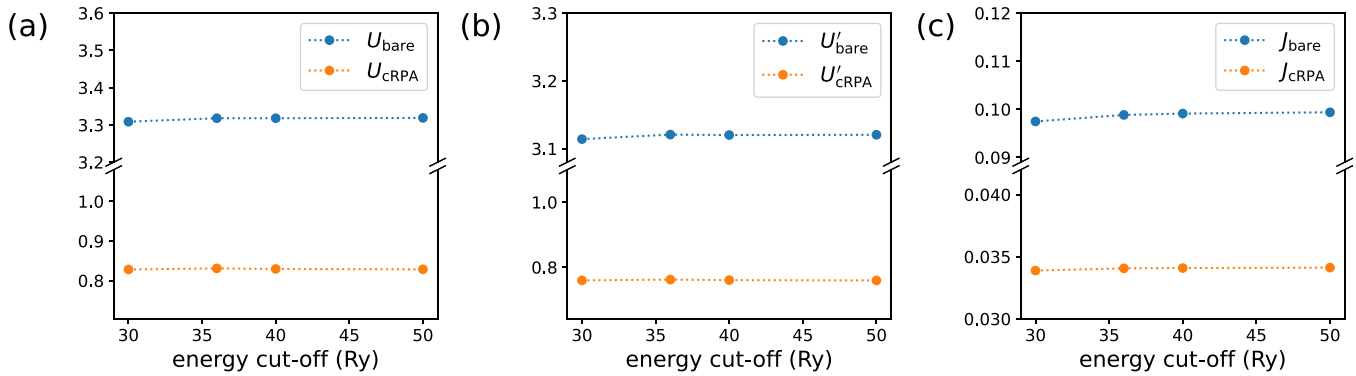

FIG. 12. The evolution of Coulomb interaction parameters with increasing energy cutoff. It can be observed that beyond 36 Ry, the changes in interaction parameters are minimal. To conserve computational resources and time, we utilized a cutoff of 36 Ry in our calculations.

greater than intraorbital interactions, implying that electron pairing within the orbitals persists even as Coulomb interactions decrease. Furthermore, the A_g mode gives $U_{ph} = U'_{ph}$, and the H_g mode gives negative J_{ph} and negative J_{eff}. Hence, H_g modes assume a pivotal role in determining the relationship $U'_{eff} = U_{eff} - 2J_{eff} > U_{eff}$; both modes are indispensable in shaping the dynamics of the superconducting mechanism.

V. CONCLUSION

In conclusion, our comprehensive *ab initio* study of a multiorbital Hubbard model coupled with phonons under varying pressure conditions sheds light on the intriguing behavior of the superconducting mechanism in K_3C_{60}. We observed significant changes in the system's parameters and theoretical concepts under increasing pressure. As pressure increased, we observed that despite the relatively smaller strength of phonon interactions, their impact on the superconducting mechanism in K_3C_{60} is significant. This is due to the local pairing with Jahn-Teller phonons [44,45,88], which is further assisted by the suppressive effect of strong Coulomb interactions on kinetic energy.

Furthermore, our study revealed that interorbital Coulomb interactions remain greater than intraorbital interactions throughout the pressure increase, indicating that electron pairing within the orbitals persists despite decreasing Coulomb interactions. Pressure-induced changes in the electronic and phononic properties of the system, along with variations in key parameters like U_{eff}, U'_{eff}, and J_{eff}, highlight the intricate interplay between different factors in the superconducting mechanism of K_3C_{60}. This study advances our understanding of unconventional superconductivity in complex materials and underscores the importance of considering both electronic and phononic contributions in such systems.

ACKNOWLEDGMENTS

This work is supported by the National Natural Science Foundation of China (Grant No. 12204130), the Shenzhen Start-Up Research Funds (Grant No. HA11409065), and the HITSZ Start-Up Funds (Grant No. X2022000). Y.N. acknowledges the support from JSPS KAKENHI (Grants No. JP23H04869 and No. JP21H01041). H.L. acknowledges support from the Fundamental Research Funds for the Central Universities of China (Grant No. 2019ZDPY16) and the Basic Research Project of Xuzhou City (Grant No. KC22043). X.Y. acknowledges support from the Natural Science Foundation of Jiangsu Province (Grant No. BK20231320).

APPENDIX: CALCULATION DETAILS OF ELECTRON-ELECTRON INTERACTIONS

In this Appendix, we demonstrate the impact of an energy cutoff on the interaction result and discuss the interaction

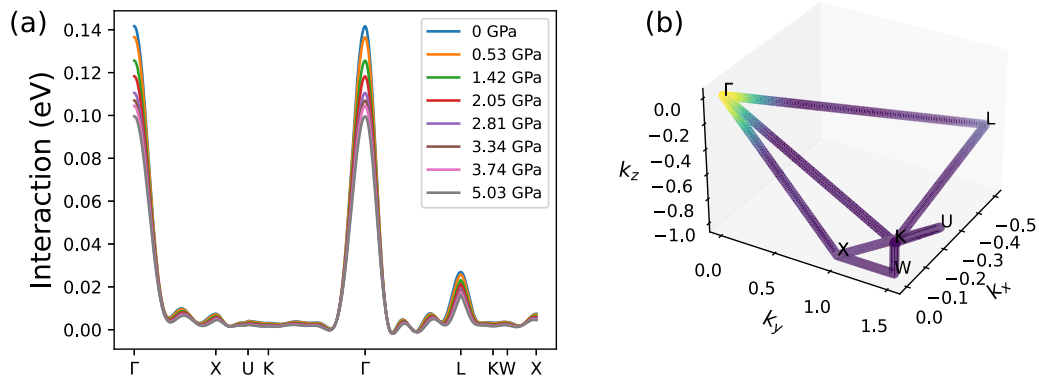

FIG. 13. (a) The on-site Coulomb repulsions at different coordinates of the Brillouin zone are presented in 2D plots for various pressures. (b) A 3D contour plot is used to depict the on-site Coulomb repulsions for a pressure of 2.81 GPa.

strength in the Brillouin zone. The cutoff is on the number of plane wave functions being utilized as basis functions to represent the wave function. Theoretically, an infinite number of basis functions is required to produce an exact answer. However, this is not computationally feasible, and a cutoff must be introduced. We used 36 Ry as the energy cutoff in the simulation. As shown in Fig. 12, the cRPA result converges to a steady value at this cutoff. In Fig. 13, we plot the Coulomb interaction strength along the high-symmetry points in a three-dimensional (3D) Brillouin zone in Fig. 13. We find that the interaction peaks at the Γ point, and the second peak is at the *L* point. With increasing pressure, the interaction shows significant decreases at the Γ point.

[1] I. V. Stankevich, M. V. Nikerov, and D. A. Bochvar, The structural chemistry of crystalline carbon: Geometry, stability, and electronic spectrum, Russ. Chem. Rev. **53**, 640 (1984).

[2] R. E. Smalley, Discovering the fullerenes, Rev. Mod. Phys. **69**, 723 (1997).

[3] R.-S. Wang, D. Peng, J.-W. Hu, L.-N. Zong, and X.-J. Chen, Orientational ordering and electron-phonon interaction in K_3C_{60} superconductor, Carbon **195**, 1 (2022).

[4] R.-S. Wang, D. Peng, L.-N. Zong, Z.-W. Zhu, and X.-J. Chen, Full set of superconducting parameters of K_3C_{60}, Carbon **202**, 325 (2023).

[5] L. Hou, X. Cui, B. Guan, S. Wang, R. Li, Y. Liu, D. Zhu, and J. Zheng, Synthesis of a monolayer fullerene network, Nature (London) **606**, 507 (2022).

[6] T. Yu, J. Li, M. Han, Y. Zhang, H. Li, Q. Peng, and H.-K. Tang, Enhancing the mechanical stability of 2D fullerene with a graphene substrate and encapsulation, Nanomaterials **13**, 1936 (2023).

[7] R. M. Tromer, L. A. Ribeiro, and D. S. Galvão, A DFT study of the electronic, optical, and mechanical properties of a recently synthesized monolayer fullerene network, Chem. Phys. Lett. **804**, 139925 (2022).

[8] L. Yu, J. Xu, B. Peng, G. Qin, and G. Su, Anisotropic optical, mechanical, and thermoelectric properties of two-dimensional fullerene networks, J. Phys. Chem. Lett. **13**, 11622 (2022).

[9] B. Peng, Monolayer fullerene networks as photocatalysts for overall water splitting, J. Am. Chem. Soc. **144**, 19921 (2022).

[10] P. Ying, H. Dong, T. Liang, Z. Fan, Z. Zhong, and J. Zhang, Atomistic insights into the mechanical anisotropy and fragility of monolayer fullerene networks using quantum mechanical calculations and machine-learning molecular dynamics simulations, Extreme Mech. Lett. **58**, 101929 (2023).

[11] H. Dong, C. Cao, P. Ying, Z. Fan, P. Qian, and Y. Su, Anisotropic and high thermal conductivity in monolayer quasi-hexagonal fullerene: A comparative study against bulk phase fullerene, Int. J. Heat Mass Transf. **206**, 123943 (2023).

[12] D. Yuan, H. Pi, Y. Jiang, Y. Hu, L. Zhou, Y. Jia, G. Su, Z. Fang, H. Weng, X. Ren, and W. Zhang, Highly in-plane anisotropic optical properties of fullerene monolayers, Sci. China: Phys. Mech. Astron. **66**, 247211 (2023).

[13] X.-D. Xiang, J. G. Hou, G. Briceño, W. A. Vareka, R. Mostovoy, A. Zettl, V. H. Crespi, and M. L. Cohen, Synthesis and electronic transport of single crystal K_3C_{60}, Science **256**, 1190 (1992).

[14] O. Klein, G. Grüner, S.-M. Huang, J. B. Wiley, and R. B. Kaner, Electrical resistivity of K_3C_{60}, Phys. Rev. B **46**, 11247(R) (1992).

[15] J. G. Hou, L. Lu, V. H. Crespi, X.-D. Xiang, A. Zettl, and M. L. Cohen, Resistivity saturation in alkali-doped C_{60}, Solid State Commun. **93**, 973 (1995).

[16] A. F. Hebard, T. T. M. Palstra, R. C. Haddon, and R. M. Fleming, Absence of saturation in the normal-state resistivity of thin films of K_3C_{60} and Rb_3C_{60}, Phys. Rev. B **48**, 9945(R) (1993).

[17] C. T. Chen, L. H. Tjeng, P. Rudolf, G. Meigs, J. E. Rowe, J. Chen, J. P. McCauley, Jr., A. B. Smith, III, A. R. McGhie, W. J. Romanow, and E. W. Plummer, Electronic states and phases of K_xC_{60} from photoemission and X-ray absorption spectroscopy, Nature (London) **352**, 603 (1991).

[18] P. J. Benning, F. Stepniak, and J. H. Weaver, Electron-diffraction and photoelectron-spectroscopy studies of fullerene and alkali-metal fulleride films, Phys. Rev. B **48**, 9086 (1993).

[19] R. Hesper, L. H. Tjeng, A. Heeres, and G. A. Sawatzky, Photoemission evidence of electronic stabilization of polar surfaces in K_3C_{60}, Phys. Rev. B **62**, 16046 (2000).

[20] W. L. Yang, V. Brouet, X. J. Zhou, H. J. Choi, S. G. Louie, M. L. Cohen, S. A. Kellar, P. V. Bogdanov, A. Lanzara, A. Goldoni, F. Parmigiani, Z. Hussain, and Z.-X. Shen, Band structure and Fermi surface of electron-doped C_{60} monolayers, Science **300**, 303 (2003).

[21] A. Cantaluppi, M. Buzzi, G. Jotzu, D. Nicoletti, M. Mitrano, D. Pontiroli, M. Riccò, A. Perucchi, P. Di Pietro, and A. Cavalleri, Pressure tuning of light-induced superconductivity in K_3C_{60}, Nat. Phys. **14**, 837 (2018).

[22] E. Rowe, B. Yuan, M. Buzzi, G. Jotzu, Y. Zhu, M. Fechner, M. Först, B. Liu, D. Pontiroli, M. Riccò, and A. Cavalleri, Resonant enhancement of photo-induced superconductivity in K_3C_{60}, Nat. Phys. **19**, 1821 (2023).

[23] K. Tanigaki, M. Kosaka, T. Manako, Y. Kubo, I. Hirosawa, K. Uchida, and K. Prassides, Alkali effects on the electronic states of K_3C_{60} and Rb_3C_{60}, Chem. Phys. Lett. **240**, 627 (1995).

[24] J. Robert, P. Petit, T. Yildirim, and J. E. Fischer, Experimental lattice dependence of the density of states in alkali fullerides, Phys. Rev. B **57**, 1226 (1998).

[25] R. Tycko, G. Dabbagh, M. J. Rosseinsky, D. W. Murphy, A. P. Ramirez, and R. M. Fleming, Electronic properties of normal and superconducting alkali fullerides probed by ^{13}C nuclear magnetic resonance, Phys. Rev. Lett. **68**, 1912 (1992).

[26] V. A. Stenger, C. H. Pennington, D. R. Buffinger, and R. P. Ziebarth, Nuclear magnetic resonance of A_3C_{60} Superconductors, Phys. Rev. Lett. **74**, 1649 (1995).

[27] C. H. Pennington and V. A. Stenger, Nuclear magnetic resonance of C_{60} and fulleride superconductors, Rev. Mod. Phys. **68**, 855 (1996).

[28] A. F. Hebard, M. J. Rosseinsky, R. C. Haddon, D. W. Murphy, S. H. Glarum, T. T. M. Palstra, A. P. Ramirez, and A. R. Kortan, Superconductivity at 18 K in potassium-doped C_{60}, Nature (London) **350**, 600 (1991).

[29] Z. Zhang, C.-C. Chen, S. P. Kelty, H. Dai, and C. M. Lieber, The superconducting energy gap of Rb_3C_{60}, Nature (London) **353**, 333 (1991).

[30] Z. Zhang, C.-C. Chen, and C. M. Lieber, Tunneling spectroscopy of M_3C_{60} superconductors: The energy gap, strong coupling, and superconductivity, Science **254**, 1619 (1991).

[31] R. F. Kiefl, W. A. MacFarlane, K. H. Chow, S. Dunsiger, T. L. Duty, T. M. S. Johnston, J. W. Schneider, J. Sonier, L. Brard, R. M. Strongin, J. E. Fischer, and A. B. Smith, Coherence peak and superconducting energy gap in Rb_3C_{60} observed by muon spin relaxation, Phys. Rev. Lett. **70**, 3987 (1993).

[32] L. C. Hebel and C. P. Slichter, Nuclear spin relaxation in normal and superconducting aluminum, Phys. Rev. **113**, 1504 (1959).

[33] S. Sasaki, A. Matsuda, and C. W. Chu, Fermi-liquid behavior and BCS *s*-wave pairing of K_3C_{60} observed by ^{13}C-NMR, J. Phys. Soc. Jpn. **63**, 1670 (1994).

[34] R. M. Fleming, A. P. Ramirez, M. J. Rosseinsky, D. W. Murphy, R. C. Haddon, S. M. Zahurak, and A. V. Makhija, Relation of structure and superconducting transition temperatures in A_3C_{60}, Nature (London) **352**, 787 (1991).

[35] G. Sparn, J. D. Thompson, S.-M. Huang, R. B. Kaner, F. Diederich, R. L. Whetten, G. Grüner, and K. Holczer, Pressure dependence of superconductivity in single-phase K_3C_{60}, Science **252**, 1829 (1991).

[36] J. E. Schirber, D. L. Overmyer, H. H. Wang, J. M. Williams, K. D. Carlson, A. M. Kini, U. Welp, and W.-K. Kwok, Pressure dependence of the superconducting transition temperature of potassium fullerene, K_xC_{60}, Physica C Superconductivity **178**, 137 (1991).

[37] R.-S. Wang, D. Peng, L.-N. Zong, L.-C. Chen, and X.-J. Chen, Variation of the critical temperature with the lattice parameter in K_3C_{60}, Carbon **199**, 181 (2022).

[38] O. Zhou, Q. Zhu, J. E. Fischer, N. Coustel, G. B. M. Vaughan, P. A. Heiney, J. P. McCauley, Jr., and A. B. Smith, III, Compressibility of M_3C_{60} fullerene superconductors: Relation between T_c and lattice parameter, Science **255**, 833 (1992).

[39] M. J. Rosseinsky, A. P. Ramirez, S. H. Glarum, D. W. Murphy, R. C. Haddon, A. F. Hebard, T. T. M. Palstra, A. R. Kortan, S. M. Zahurak, and A. V. Makhija, Superconductivity at 28 K in Rb_xC_{60}, Phys. Rev. Lett. **66**, 2830 (1991).

[40] K. Tanigaki, I. Hirosawa, T. W. Ebbesen, J. Mizuki, Shimakawa, Y. Kubo, J. S. Tsai, and S. Kuroshima, Superconductivity in sodium-and lithium-containing alkali-metal fullerides, Nature (London) **356**, 419 (1992).

[41] Y. Yildirim, J. E. Fischer, R. Dinnebier, P. W. Stephens, and C. L. Lin, Fulleride superconductors and orientational order: T_c vs lattice constant in $Na_2Rb_xCs_{1-x}C_{60}$, Solid State Commun. **93**, 269 (1995).

[42] T. Takahashi, S. Suzuki, T. Morikawa, H. Katayama-Yoshida, S. Hasegawa, H. Inokuchi, K. Seki, K. Kikuchi, S. Suzuki, K. Ikemoto, and Y. Achiba, Pseudo-gap at the Fermi level in K_3C_{60} observed by photoemission and inverse photoemission, Phys. Rev. Lett. **68**, 1232 (1992).

[43] S. C. Tiwari, A. Kashyap, A. K. Surana, R. K. Paliwal, and S. L. Kakani, Polaronic mechanism of superconductivity in doped fulleride systems, Int. J. Mod. Phys. B **23**, 615 (2009).

[44] J. E. Han, O. Gunnarsson, and V. H. Crespi, Strong superconductivity with local Jahn-Teller phonons in C_{60} solids, Phys. Rev. Lett. **90**, 167006 (2003).

[45] Y. Nomura, S. Sakai, M. Capone, and R. Arita, Exotic *s*-wave superconductivity in alkali-doped fullerides, J. Phys.: Condens. Matter **28**, 153001 (2016).

[46] M. Capone, M. Fabrizio, C. Castellani, and E. Tosatti, Strongly correlated superconductivity, Science **296**, 2364 (2002).

[47] Y. Nomura, S. Sakai, M. Capone, and R. Arita, Unified understanding of superconductivity and Mott transition in alkali-doped fullerides from first principles, Sci. Adv. **1**, e1500568 (2015).

[48] H.-C. Jiang and S. Kivelson, Electronic pair binding and Hund's rule violations in doped C_{60}, Phys. Rev. B **93**, 165406 (2016).

[49] G. Kotliar, S. Y. Savrasov, K. Haule, V. S. Oudovenko, O. Parcollet, and C. A. Marianetti, Electronic structure calculations with dynamical mean-field theory, Rev. Mod. Phys. **78**, 865 (2006).

[50] K. Held, Electronic structure calculations using dynamical mean field theory, Adv. Phys. **56**, 829 (2007).

[51] M. Imada and T. Miyake, Electronic structure calculation by first principles for strongly correlated electron systems, J. Phys. Soc. Jpn. **79**, 112001 (2010).

[52] F. Aryasetiawan, M. Imada, A. Georges, G. Kotliar, S. Biermann, and A. I. Lichtenstein, Frequency-dependent local interactions and low-energy effective models from electronic structure calculations, Phys. Rev. B **70**, 195104 (2004).

[53] Y. Nomura, K. Nakamura, and R. Arita, Effect of electron-phonon interactions on orbital fluctuations in iron-based superconductors, Phys. Rev. Lett. **112**, 027002 (2014).

[54] Y. Nomura and R. Arita, *Ab initio* downfolding for electron-phonon-coupled systems: Constrained density-functional perturbation theory, Phys. Rev. B **92**, 245108 (2015).

[55] Y. Nomura, K. Nakamura, and R. Arita, *Ab initio* derivation of electronic low-energy models for C_{60} and aromatic compounds, Phys. Rev. B **85**, 155452 (2012).

[56] N. Marzari and D. Vanderbilt, Maximally localized generalized Wannier functions for composite energy bands, Phys. Rev. B **56**, 12847 (1997).

[57] K. Momma and F. Izumi, VESTA: A three-dimensional visualization system for electronic and structural analysis, J. Appl. Cryst. **41**, 653 (2008).

[58] W. Setyawan and S. Curtarolo, High-throughput electronic band structure calculations: Challenges and tools, Comput. Mater. Sci. **49**, 299 (2010).

[59] P. Giannozzi, O. Baseggio, P. Bonfà, D. Brunato, R. Car, I. Carnimeo, C. Cavazzoni, S. de Gironcoli, P. Delugas, F. Ferrari Ruffino, A. Ferretti, N. Marzari, I. Timrov, A. Urru, and S. Baroni, Quantum ESPRESSO toward the exascale, J. Chem. Phys. **152**, 154105 (2020).

[60] P. Giannozzi, O. Andreussi, T. Brumme, O. Bunau, M. Buongiorno Nardelli, M. Calandra, R. Car, C. Cavazzoni, D. Ceresoli, M. Cococcioni *et al.*, Advanced capabilities for materials modelling with Quantum ESPRESSO, J. Phys.: Condens. Matter **29**, 465901 (2017).

[61] P. Giannozzi, S. Baroni, N. Bonini, M. Calandra, R. Car, C. Cavazzoni, D. Ceresoli, G. L. Chiarotti, M. Cococcioni, I. Dabo *et al.*, QUANTUM ESPRESSO: A modular and open-source software project for quantum simulations of materials, J. Phys.: Condens. Matter **21**, 395502 (2009).

[62] T. Fujiwara, S. Yamamoto, and Y. Ishii, Generalization of the iterative perturbation theory and metal–insulator transition in multi-orbital Hubbard bands, J. Phys. Soc. Jpn. **72**, 777 (2003).

[63] Y. Nohara, S. Yamamoto, and T. Fujiwara, Electronic structure of perovskite-type transition metal oxides $LaMO_3$(M = Ti ∼ Cu) by U + GW approximation, Phys. Rev. B **79**, 195110 (2009).

[64] K. Nakamura, R. Arita, and M. Imada, *Ab initio* derivation of low-energy model for iron-based superconductors LaFeAsO and LaFePO, J. Phys. Soc. Jpn. **77**, 093711 (2008).

[65] K. Nakamura, Y. Yoshimoto, T. Kosugi, R. Arita, and M. Imada, *Ab initio* derivation of low-energy model for κ-ET type organic conductors, J. Phys. Soc. Jpn. **78**, 083710 (2009).

[66] K. Nakamura, Y. Nohara, Y. Yosimoto, and Y. Nomura, *Ab initio* GW plus cumulant calculation for isolated band systems: Application to organic conductor $(TMTSF)_2PF_6$ and transition-metal oxide $SrVO_3$, Phys. Rev. B **93**, 085124 (2016).

[67] K. Nakamura, Y. Yoshimoto, Y. Nomura, T. Tadano, M. Kawamura, T. Kosugi, K. Yoshimi, T. Misawa, and Y. Motoyama, RESPACK: An *ab initio* tool for derivation of effective low-energy model of material, Comput. Phys. Commun. **261**, 107781 (2021).

[68] P. A. Heiney, J. E. Fischer, A. R. McGhie, W. J. Romanow, A. M. Denenstein, J. P. McCauley, Jr., A. B. Smith, and D. E. Cox, Orientational ordering transition in solid C_{60}, Phys. Rev. Lett. **66**, 2911 (1991).

[69] J. E. Fischer and P. A. Heiney, Order and disorder in fullerene and fulleride solids, J. Phys. Chem. Solids **54**, 1725 (1993).

[70] A. Georges, G. Kotliar, W. Krauth, and M. J. Rozenberg, Dynamical mean-field theory of strongly correlated fermion systems and the limit of infinite dimensions, Rev. Mod. Phys. **68**, 13 (1996).

[71] G. R. Darling, A. Y. Ganin, M. J. Rosseinsky, Y. Takabayashi, and K. Prassides, Intermolecular overlap geometry gives two classes of fulleride superconductor: Electronic structure of 38 K $T_c Cs_3C_{60}$, Phys. Rev. Lett. **101**, 136404 (2008).

[72] O. Gunnarsson, Superconductivity in fullerides, Rev. Mod. Phys. **69**, 575 (1997).

[73] V. P. Antropov, O. Gunnarsson, and A. I. Liechtenstein, Phonons, electron-phonon, and electron-plasmon coupling in C_{60} compounds, Phys. Rev. B **48**, 7651 (1993).

[74] T. W. Ebbesen, J. S. Tsai, K. Tanigaki, H. Hiura, Y. Shimakawa, Y. Kubo, I. Hirosawa, and J. Mizuki, Dopant isotope effect on superconductivity in Rb_3C_{60}, Physica C: Superconductivity **203**, 163 (1992).

[75] B. Burk, V. H. Crespi, M. S. Fuhrer, A. Zettl, and M. L. Cohen, Alkali-metal isotope effect in Rb_3C_{60}, Physica C: Superconductivity **235–240**, 2493 (1994).

[76] B. Burk, V. H. Crespi, A. Zettl, and M. L. Cohen, Rubidium isotope effect in superconducting Rb_3C_{60}, Phys. Rev. Lett. **72**, 3706 (1994).

[77] C. Christides, D. A. Neumann, K. Prassides, J. R. D. Copley, J. J. Rush, M. J. Rosseinsky, D. W. Murphy, and R. C. Haddon, Neutron-scattering study of $C_{60}{}^{n-}$ ($n = 3, 6$) librations in alkali-metal fullerides, Phys. Rev. B **46**, 12088(R) (1992).

[78] W. E. Pickett, D. A. Papaconstantopoulos, M. R. Pederson, and S. C. Erwin, Electron-phonon coupling in A_3C_{60}: Contributions from intermolecular modes, J. Supercond. **7**, 651 (1994).

[79] K. Prassides, C. Christides, M. J. Rosseinsky, J. Tomkinson, D. W. Murphy, and R. C. Haddon, Neutron spectroscopy and electron-phonon coupling in alkali-metal-doped fullerides, Europhys. Lett. **19**, 629 (1992).

[80] C. M. Varma, J. Zaanen, and K. Raghavachari, Superconductivity in the fullerenes, Science **254**, 989 (1991).

[81] M. Lannoo, G. A. Baraff, M. Schlüter, and D. Tomanek, Jahn-Teller effect for the negatively charged C_{60} molecule: Analogy with the silicon vacancy, Phys. Rev. B **44**, 12106(R) (1991).

[82] O. Gunnarsson, *Alkali-Doped Fullerides: Narrow-Band Solids with Unusual Properties* (World Scientific, Singapore, 2004).

[83] A. Y. Ganin, Y. Takabayashi, P. Jeglič, D. Arčon, A. Potočnik, P. J. Baker, Y. Ohishi, M. T. McDonald, M. D. Tzirakis, A. McLennan, G. R. Darling, M. Takata, M. J. Rosseinsky, and K. Prassides, Polymorphism control of superconductivity and magnetism in Cs_3C_{60} close to the Mott transition, Nature (London) **466**, 221 (2010).

[84] H. R. Naren, A. Thamizhavel, A. K. Nigam, and S. Ramakrishnan, Strongly correlated superconductivity in $Rh_{17}S_{15}$, Phys. Rev. Lett. **100**, 026404 (2008).

[85] M. Capone, M. Fabrizio, C. Castellani, and E. Tosatti, Colloquium: Modeling the unconventional superconducting properties of expanded A_3C_{60} fullerides, Rev. Mod. Phys. **81**, 943 (2009).

[86] M. Capone, M. Fabrizio, and E. Tosatti, Direct transition between a singlet Mott insulator and a superconductor, Phys. Rev. Lett. **86**, 5361 (2001).

[87] M. Capone, M. Fabrizio, C. Castellani, and E. Tosatti, Strongly correlated superconductivity and pseudogap phase near a multiband Mott insulator, Phys. Rev. Lett. **93**, 047001 (2004).

[88] O. Gunnarsson, H. Handschuh, P. S. Bechthold, B. Kessler, G. Ganteför, and W. Eberhardt, Photoemission spectra of $C_{60}{}^-$: Electron-phonon coupling, Jahn-Teller effect, and superconductivity in the fullerides, Phys. Rev. Lett. **74**, 1875 (1995).

[89] F. C. Zhang, M. Ogata, and T. M. Rice, Attractive interaction and superconductivity for K_3C_{60}, Phys. Rev. Lett. **67**, 3452 (1991).